Can we relate the surface expression of dike-induced normal faults to subsurface dike geometry?

Craig Magee[1] and Christopher A-L Jackson[2]

[1]Institute of Geophysics and Tectonics, School of Earth Science and Environment, University of Leeds, Leeds, LS2 9JT, UK

[2]Basins Research Group (BRG), Department of Earth Science and Engineering, Imperial College, London, SW7 2BP, UK

Dikes feed volcanic eruptions and drive crustal extension on Earth and other planetary bodies. Yet many dikes do not reach the surface, instead triggering normal faulting and graben formation in overlying rock. Whilst dike-induced faults provide a surficial and accessible record of active and ancient diking, unlocking these archives is difficult because we do not know how faults grow above or geometrically relate to dikes. We use seismic reflection data to quantify the 3D structure and kinematics of natural dike-induced faults, and test how their surface expression relates to dike geometry. We show dike-induced faults are non-planar, indicating fault dips measured at the surface cannot be projected downwards and used, along with graben half-width, to estimate dike depth. We also show multiple displacement maxima occur across individual dike-induced faults but never at their upper tips, suggesting the total extension accommodated by faulting, an assumed proxy for dike thickness, cannot be calculated by measuring fault heave at the surface. The observed displacement distribution is consistent with nucleation and linkage of isolated faults between the dike upper tip and surface, perhaps in response to cyclical stalling, thickening, and

propagation of a laterally intruded dike. Our results demonstrate at-surface measurements of dike-induced faults cannot be used to estimate dike parameters without a priori knowledge of fault structure and kinematics. We show reflection seismology is a powerful tool for studying how faults grow above dikes, and anticipate future seismic-based studies will improve our understanding of dike emplacement and its translation into surface deformation.

INTRODUCTION

Field observations, geodetic data, and seismicity show igneous dike intrusion can induce normal faulting of overlying rock (e.g., Pollard et al., 1983; Passarelli et al., 2015; Trippanera et al., 2015a; Xu et al., 2016). Dike-induced normal faults form pairs that dip towards underlying dikes and bound dike-parallel graben (Fig. 1) (e.g., Mastin and Pollard, 1988; Trippanera et al., 2015b). Faulting occurs because dike intrusion and dilation perturbs overburden stresses, concentrating tensile stress in two lobes above the dike tip and two zones at the free surface, promoting failure (Fig. 1) (e.g., Pollard et al., 1983; Rubin and Pollard, 1988; Rubin, 1992; Koehn et al., 2019). Because diking drives the stress changes promoting faulting, dike emplacement and shape thus control the growth and geometry of dike-induced faults (e.g., Pollard et al., 1983; Rubin and Pollard, 1988; Dumont et al., 2016; Dumont et al., 2017). By inverting dike-induced fault properties (e.g., heave) we can: (i) track intruding dikes (e.g., Pallister et al., 2010); (ii) estimate dike volumes and thus infer melt conditions (e.g., Wilson and Head, 2002); and (iii) examine how diking shapes Earth and other planetary bodies (e.g., Bull et al., 2003; Schultz et al., 2004; Carbotte et al., 2006; Ruch et al., 2016). However, we are typically restricted to investigating surface expressions of dike-induced faults (e.g., Schultz et al., 2004; Trippanera et al., 2015a; Dumont et al., 2016), meaning 3D physical and numerical models of these systems cannot easily be verified (e.g., Mastin and Pollard, 1988; Trippanera et al., 2015b; Koehn et al., 2019).

Here we use seismic reflection data, from offshore NW Australia that image the 3D structure of the newly discovered, laterally emplaced Exmouth Dyke Swarm and an array of dike-induced faults (Magee and Jackson, 2020). We present the first 3D analysis quantifying relationships between natural dikes and dike-induced faults, and specifically test: (i) whether graben half-width geometrically relates to and can be used to predict the subsurface depth of a dikes upper tip (e.g., Wilson and Head, 2002; Trippanera et al., 2015b; Hjartardóttir et al., 2016); and (ii) if extension accommodated by dike-induced faults is sensitive to dike thickness, such that fault heaves measured at the surface can be related to dike thickness (e.g., Rubin and Pollard, 1988; Rubin, 1992; Trippanera et al., 2015b). Our data also informs debate regarding the vertical extent and growth of dike-induced faults, which are hypothesized to nucleate either: (i) as near-surface vertical fractures, some distance *above* the dike tip (Fig. 1A) (Trippanera et al., 2015a; Trippanera et al., 2015b; Al Shehri and Gudmundsson, 2018); (ii) *at* dike tips (Fig. 1B) (Rubin, 1992; Xu et al., 2016; Koehn et al., 2019); (iii) a combination of (i) and (ii) (Fig. 1C) (Tentler, 2005; Rowland et al., 2007); (iv) *between* the dyke tip and surface (Fig. 1D) (Mastin and Pollard, 1988; Koehn et al., 2019); or (v) in front of a laterally propagating dike, eventually being cross-cut by the dike (Fig. 1E) (Rubin and Pollard, 1988; Bull et al., 2003; Rowland et al., 2007). These growth models can be used to predict diagnostic fault displacement-depth trends, if we consider displacement is presently greatest where faults initially nucleated (Fig. 1) (Trippanera et al., 2015b; Magee et al., 2019); these predictions show surface offset by dike-induced faults is influenced by their kinematics. Measuring 3D displacement patterns across dike-induced faults allows us to reconstruct their kinematics, which we can relate to dike thickness changes and emplacement mechanics. By unravelling how dike emplacement translates into faulting, we provide critical insights into the inversion of dike geometry from surface-based analyses of dike-induced faults on Earth and other planetary bodies.

DATASET AND METHODS

The time-migrated Chandon 3D seismic reflection survey has a bin spacing of 25 m and a record length of 6 s two-way time (TWT). We present images in which a trough (black) reflection corresponds to a downward increase in acoustic impedance whilst a peak (white) reflection represents a downward decrease in acoustic impedance. We use velocity information from four boreholes to convert the seismic data, down to 4 s TWT, from depth in ms TWT to metres (Fig. 2; Supplementary Files 1 and 2). Using the velocity data (±10 %), coupled with dominant frequency measurements (±10 %), we calculate the limits of separability and visibility. For the strata hosting the dike-induced faults, the limits of separability and visibility are ~20±4 m and ~3±1 m, respectively (Supplementary File 3).

Quantitative Analysis

We analysed faults EF1 and EF2 because they are continuous along-strike, show little interaction with tectonic (i.e. dike-unrelated) faults, and their northernmost lateral tips are imaged in our data (Fig. 2A). We mapped 11 seismic horizons (i.e. HA–HK; Fig. 2C) around EF1 and EF2 and identified hanging wall and footwall cut-offs of each horizon along fault-perpendicular transects every 125 m along-strike. Where horizons are folded adjacent to the faults, which may reflect ductile strain, we projected the regional trend of the strata to define cut-offs (Mansfield and Cartwright, 1996). For each cut-off pair, we measured fault throw and extracted fault dip (α); this data was used to calculate fault heave and displacement (Supplementary File 4). We lack pre-kinematic piercing points (e.g., channels) to determine whether faulting was oblique- or dip-slip, so we assume displacement was dip-slip. Graben half-width (HW) was measured every 125 m along-strike on HF, the uppermost prominent reflection that both EF1 and EF2 displace along their lengths, and use with α to predict the depth to the dike tip (*D'*). We measured actual dike upper tip depths (*D*) beneath HF every 250 m along-strike. Although HF does not mark the top of the faults and thus does not represent their contemporaneous surface expression, testing whether *D'* is a realistic proxy for *D* can be conducted at any structural level within dike-induced graben. The thickness of the dike's seismic expression at ~4 km depth was also measured every 250 m along-strike. Data for *HW* and dike thickness are presented with ±5% errors, accounting for human imprecision, whereas the *D*, *α*, displacement, and heave measurements assume errors are ±15%, given they also contain errors associated with depth-conversion (see Supplementary File 5 and Magee and Jackson, 2020).

DIKES AND DIKE-INDUCED FAULTS

Dikes (A-I) manifest as broadly planar, ~NNE-trending, low-amplitude zones that disrupt sub-horizontal stratigraphic reflections (Fig. 2) (Magee and Jackson, 2020). Above and parallel to the dikes are ~NNE-trending, ~1–2 km wide graben bound by low-displacement (i.e. <150 m), normal faults that converge on the dike upper tips (Fig. 2) (Magee and Jackson, 2020). The faults displace a ~1 km thick, clastic-dominated sequence and, at their upper tips, offset the ~148 Myr Base Cretaceous unconformity (HK; Fig. 2C). Displacement of HK, but not overlying strata, suggests faulting, and thus dyking, occurred during the Late Jurassic (Fig. 2C) (Magee and Jackson, 2020). We examine an ~18 km long section of a graben bound by EF1 and EF2, and underlain by Dike E (Fig. 2). Dike E displays two subtle but abrupt changes in strike, an apparent northwards decrease in thickness, and extends for >5 km beyond the northern limits of EF1 and EF2 (Fig. 2).

Graben Half-width And Dike Depth

Graben half-width (*HW*) is used to predict a dike's upper tip depth (*D'*) beneath the surface by assuming that fault dip (α) remains constant with depth (i.e. $D' = HW \tan \alpha$) (e.g., Pollard et al., 1983; Trippanera et al., 2015b; Hjartardóttir et al., 2016). We show *HW* ranges from ~366±18 m to 728±36 m (Fig. 3A). The southern ~8 km of the graben is characterised by a mean *HW* of ~488±24 m, which abruptly increases to ~711±36 m where the average dip of both faults at HF (HFα) decreases from ~56° to ~45° (Figs 3A and B). Our predicted *D'* values range from ~446±46 m to ~1006±106 m.

Our 3D seismic data allow us to test the accuracy of *D'* because they image and thus allow measurement of *D*. We show *D* ranges from ~493±80 m to 896±134 m and is positively, yet only weakly ($R^2 = 0.20$) correlated to *D'* (Fig. 3C). *D'* can exceed *D* by up to 350±145 m (Fig. 3C). We acknowledge there is broadly a good agreement between *D'* and *D* if error ranges are considered (Fig. 3C), and that the true location of upper dike tips may be shallower than resolved. However, because *D'* is sensitive to fault dip, we suggest the variation in dip recorded both along-strike and down-dip of EF1 and EF2 (Fig. 3B) may also explain discrepancies between *D'* and *D*. For example, where the dips of EF1 and EF2 measured at HA–HE are less than at HF (i.e. HFα - HE–HAα >0), the faults are concave-up (listric) and *D'* overestimates *D* (*D*:*D'*<1; Fig. 3D). Conversely, where faults are convex-up (i.e. HFα - HE–HAα <0), *D'* underestimates *D* (*D*:*D'*>1; Fig. 3D). Offset of dike-induced faults by tectonic faults can also cause *D'* to deviate from *D* by increasing or decreasing *HW* (e.g., Fig. 3A).

Dike-induced Fault Displacement And Kinematics

Displacement varies along-strike and down-dip of both EF1 and EF2, which have displacement maxima of ~73±11 m and ~113±17 m, respectively, with EF2 accommodating more strain (Figs 4A and B). Local displacement maxima (e.g. segments 1–3 on EF2) occur at different structural levels and are not typically positioned at the same along-strike location (Figs 4A and B). Cumulative heave across both EF1 and EF2 is up to ~115±17 m and broadly decreases northwards, consistent with a reduction in the thickness of Dike E's seismic expression (Fig. 2D). Displacement-depth profiles are complex but occasionally display clear 'M-shaped' or 'C-shaped' trends (cf. Figs 1 and 4D) (e.g., Muraoka and Kamata, 1983). Displacement maxima rarely occur at the lower tips of EF1 and EF2 and never at their upper tips (Figs 4A and D).

Dike-induced Fault Kinematics And Dike Emplacement

Dike-induced fault displacement is intrinsically linked to dike dilation (e.g., Tryggvason, 1984; Rubin, 1992), suggesting variations in dike thickness are related to the amount of displacement across EF1 and EF2. Such changes in dike thickness could be controlled by localised inelastic deformation of the host rock (e.g., fluidisation or thermal erosion), variations in host rock mechanical properties, and/or lateral pressure gradients generated in response to loading conditions or magma properties (e.g., Kavanagh and Sparks, 2011; Gudmundsson et al., 2012; Vachon and Hieronymus, 2017). If zones of high displacement on EF1 and EF2 define where these dike-induced faults nucleated (e.g., Cartwright et al., 1995; Trippanera et al., 2015b; Deng et al., 2017), the present distribution of these zones implies isolated faults develop above the thickest dike portions, between the dike tip and contemporaneous surface (Mastin and Pollard, 1988; Koehn et al., 2019), *during* lateral propagation of the underlying dike (Magee and Jackson, 2020). To nucleate dike-induced faults at discrete intervals along-strike during lateral emplacement, we suggest that (Fig. 4E): (i) fault nucleation and growth could occur in response to dike propagation, but may be enhanced when the dike stalls, pressurizes, and thickens (e.g., Sigmundsson et al., 2015); (ii) renewed dike propagation, facilitated by magma breaking out from the dike nose (Healy et al., 2018), could instigate nucleation of a new, laterally offset fault segment; and (iii) continued intrusion and dike dilation may lead to fault growth and coalescence. Alternatively, zones of high displacement may develop *after* dike emplacement, above areas where the dike becomes locally thickened (e.g., by wall rock erosion); i.e. the present displacement distribution may be unrelated to fault nucleation, but instead reflect post-emplacement dike processes, such as dike widening due to wall rock erosion (Fig. 4F).

DISCUSSION

We show pairs of natural dike-induced faults extend from the contemporaneous surface and converge on, but do not continue below, a dikes upper tip. Displacement varies across the dike-induced faults, likely reflecting changes in the thickness of the underlying dike. If zones of high displacement correspond to fault nucleation sites, our results indicate the dike-induced faults nucleated between the dike and contemporaneous surface (Mastin and Pollard, 1988; Koehn et al., 2019); this contrasts with many existing models, which suggest dike-induced faults nucleate either at the surface and/or upper dike tip (e.g., Rubin and Pollard, 1988; Rubin, 1992; Tentler, 2005; Trippanera et al., 2015b; Al Shehri and Gudmundsson, 2018). Regardless of where the faults nucleated, our kinematic reconstruction implies any seismicity generated by this type of dike-induced faulting is likely to be concentrated away from the dike upper tip, in areas where most displacement is initially accrued. We also demonstrate the distribution of displacement across dike-induced faults influences their surface expression, such that fault heave measured along the syn-intrusion surface likely does not approximate dike thickness (e.g., Rubin and Pollard, 1988; Rubin, 1992; Trippanera et al., 2015b). Similarly, we show fault dip varies down-dip, implying dike upper tip depths estimated from graben half-width, which commonly assume faults are planar, may be incorrect (cf. Wilson and Head, 2002; Trippanera et al., 2015b; Hjartardóttir et al., 2016).

Accurately constraining dike parameters (e.g., thickness and depth) from the surface expression of dike-induced faults thus requires knowledge of fault geometry and kinematics in 3D; unfortunately this information is commonly unavailable. Using seismic reflection data to unravel how faults grow above dikes and quantify their 3D structure can improve our understanding of dike emplacement.

ACKNOWLEDGEMENTS

CM is funded by a NERC Independent Research Fellowship (NE/R014086/1). We are grateful to Geoscience Australia for making data used in this study publicly available (http://www.ga.gov.au/nopims). Schlumberger are thanked for provision of Petrel software. We thank Meredith Townsend, Agust Gudmundsson, Jonathan Bull, and two anonymous reviewers for their constructive contribution to previous versions of this manuscript.

FIGURE CAPTIONS

Figure 1: Predicted displacement patterns for different models of dike-induced faulting; see text for details. Horizontal stress patterns above an intruding dike, showing concentrated tensile stress at the surface (i) and above the dike tip (ii), are also shown (Rubin and Pollard, 1988); note schematics only depict one half of a dike.

Figure 2: (A) HF depth-structure map showing dike-induced faults and underlying dike traces. Four boreholes shown are: 1=Chandon-1; 2=Chandon-2; 3=Chandn-3; 4=Yellowglen-1. Inset: Location map of Chandon 3D survey. (B) Root-mean squared (RMS) amplitude extraction across a ~0.2 km high window centred at ~4 km depth showing dike A–I traces. (C) Depth-converted, vertically exaggerated (VE) seismic section showing dikes, faults, and key horizons; see (A) for location. (D) Dike E thickness changes with distance. See

Supplementary File 6 for uninterpreted version. A video of the data and our seismic interpretations is provided in Supplementary File 7.

Figure 3: (A) RMS amplitude map (of HF) and graph showing variations in graben half-width (*HW*) along-strike. Dip variations at HF (HFα), as well as measured (*D*) and predicted (*D'*) dike tip depth below HF also plotted. Error bars for *HW* are ±5% and error envelopes for *D* and *D'* are ±15%. (B) Fault dip map. (C) Plot showing *D'* may not equal *D*; error bars are ±15%. (D) Plot of *D*:*D'* against HFα - HE–HAα.

Figure 4: (A) Displacement distribution map across EF1 and EF2. (B and C) Plots of maximum displacement and heave, respectively, along EF2 and EF2; cumulative maximum displacement and heave combining data from both faults also shown. Error bars are ±15%. (D) Depth-displacement profiles for EF1 and EF2; error bars are ±15%. See (A) for locations. (E and F) Conceptual models for dike-induced faults development during and after dike emplacement.

REFERENCES

Al Shehri, A., and Gudmundsson, A., 2018, Modelling of surface stresses and fracturing during dike emplacement: Application to the 2009 episode at Harrat Lunayyir, Saudi Arabia: Journal of Volcanology and Geothermal Research, v. 356, p. 278-303.

Bull, J. M., Minshull, T. A., Mitchell, N. C., Thors, K., Dix, J. K., and Best, A. I., 2003, Fault and magmatic interaction within Iceland's western rift over the last 9kyr: Geophysical Journal International, v. 154(1), p. F1-F8.

Carbotte, S. M., Detrick, R. S., Harding, A., Canales, J. P., Babcock, J., Kent, G., Van Ark, E., Nedimovic, M., and Diebold, J., 2006, Rift topography linked to magmatism at the intermediate spreading Juan de Fuca Ridge: Geology, v. 34, no. 3, p. 209-212.

Cartwright, J. A., Trudgill, B. D., and Mansfield, C. S., 1995, Fault growth by segment linkage: an explanation for scatter in maximum displacement and trace length data from the Canyonlands Grabens of SE Utah: Journal of Structural Geology, v. 17, no. 9, p. 1319-1326.

Deng, C., Gawthorpe, R. L., Finch, E., and Fossen, H., 2017, Influence of a pre-existing basement weakness on normal fault growth during oblique extension: Insights from discrete element modeling: Journal of Structural Geology, v. 105, p. 44-61.

Dumont, S., Klinger, Y., Socquet, A., Doubre, C., and Jacques, E., 2017, Magma influence on propagation of normal faults: Evidence from cumulative slip profiles along Dabbahu-Manda-Hararo rift segment (Afar, Ethiopia): Journal of Structural Geology, v. 95, p. 48-59.

Dumont, S., Socquet, A., Grandin, R., Doubre, C., and Klinger, Y., 2016, Surface displacements on faults triggered by slow magma transfers between dike injections in the 2005–2010 rifting episode at Dabbahu–Manda–Hararo rift (Afar, Ethiopia): Geophysical Journal International, v. 204, no. 1, p. 399-417.

Gudmundsson, A., Kusumoto, S., Simmenes, T. H., Philipp, S. L., Larsen, B., and Lotveit, I. F., 2012, Effects of overpressure variations on fracture apertures and fluid transport: Tectonophysics, v. 581, p. 220-230.

Healy, D., Rizzo, R., Duffy, M., Farrell, N. J., Hole, M. J., and Muirhead, D., 2018, Field evidence for the lateral emplacement of igneous dikes: Implications for 3D mechanical models and the plumbing beneath fissure eruptions: Volcanica, v. 1, no. 2, p. 85-105.

Hjartardóttir, Á. R., Einarsson, P., Gudmundsson, M. T., and Högnadóttir, T., 2016, Fracture movements and graben subsidence during the 2014 Bárðarbunga dike intrusion in Iceland: Journal of Volcanology and Geothermal Research, v. 310, p. 242-252.

Kavanagh, J., and Sparks, R. S. J., 2011, Insights of dike emplacement mechanics from detailed 3D dike thickness datasets: Journal of the Geological Society, v. 168, no. 4, p. 965-978.

Koehn, D., Steiner, A., and Aanyu, K., 2019, Modelling of extension and dyking-induced collapse faults and fissures in rifts: Journal of Structural Geology, v. 118, p. 21-31.

Magee, C., Ernst, R. E., Muirhead, J., Phillips, T., and Jackson, C. A.-L., 2019, Magma Transport Pathways in Large Igneous Provinces: Lessons from Combining Field Observations and Seismic Reflection Data, *in* Srivastava, R., Ernst, R., and Peng, P., eds., Dike Swarms of the World: A Modern Perspective, Springer, p. 45-85.

Magee, C., and Jackson, C. A-L., 2020, Seismic reflection data reveal the 3D structure of the newly discovered Exmouth Dyke Swarm, offshore NW Australia: Solid Earth, v. 11, p. 579-606.

Mansfield, C. S., and Cartwright, J. A., 1996, High resolution fault displacement mapping from three-dimensional seismic data: evidence for dip linkage during fault growth: Journal of Structural Geology, v. 18, p. 249-263.

Mastin, L. G., and Pollard, D. D., 1988, Surface deformation and shallow dike intrusion processes at Inyo Craters, Long Valley, California: Journal of Geophysical Research: Solid Earth, v. 93, no. B11, p. 13221-13235.

Muraoka, H., and Kamata, H., 1983, Displacement distribution along minor fault traces: Journal of Structural Geology, v. 5, no. 5, p. 483-495.

Pallister, J. S., McCausland, W. A., Jónsson, S., Lu, Z., Zahran, H. M., El Hadidy, S., Aburukbah, A., Stewart, I. C., Lundgren, P. R., and White, R. A., 2010, Broad accommodation of rift-related extension recorded by dike intrusion in Saudi Arabia: Nature Geoscience, v. 3, no. 10, p. 705-712.

Passarelli, L., Rivalta, E., Cesca, S., and Aoki, Y., 2015, Stress changes, focal mechanisms, and earthquake scaling laws for the 2000 dike at Miyakejima (Japan): Journal of Geophysical Research: Solid Earth, v. 120, no. 6, p. 4130-4145.

Pollard, D. D., Delaney, P. T., Duffield, W. A., Endo, E. T., and Okamura, A. T., 1983, Surface deformation in volcanic rift zones: Tectonophysics, v. 94, no. 1-4, p. 541-584.

Rowland, J., Baker, E., Ebinger, C., Keir, D., Kidane, T., Biggs, J., Hayward, N., and Wright, T., 2007, Fault growth at a nascent slow-spreading ridge: 2005 Dabbahu rifting episode, Afar: Geophysical Journal International, v. 171, no. 3, p. 1226-1246.

Rubin, A. M., 1992, Dike-induced faulting and graben subsidence in volcanic rift zones: Journal of Geophysical Research: Solid Earth, v. 97, no. B2, p. 1839-1858.

Rubin, A. M., and Pollard, D. D., 1988, Dike-induced faulting in rift zones of Iceland and Afar: Geology, v. 16, no. 5, p. 413-417.

Ruch, J., Wang, T., Xu, W., Hensch, M., and Jónsson, S., 2016, Oblique rift opening revealed by reoccurring magma injection in central Iceland: Nature Communications, v. 7, no. 12352.

Schultz, R. A., Okubo, C. H., Goudy, C. L., and Wilkins, S. J., 2004, Igneous dikes on Mars revealed by Mars orbiter laser altimeter topography: Geology, v. 32, no. 10, p. 889-892.

Sigmundsson, F., Hooper, A., Hreinsdóttir, S., Vogfjörd, K. S., Ófeigsson, B. G., Heimisson, E. R., Dumont, S., Parks, M., Spaans, K., and Gudmundsson, G. B., 2015, Segmented lateral dike growth in a rifting event at Bárðarbunga volcanic system, Iceland: Nature, v. 517, no. 7533, p. 191-195.

Symonds, P. A., Planke, S., Frey, O., and Skogseid, J., 1998, Volcanic evolution of the Western Australian Continental Margin and its implications for basin development: The Sedimentary Basins of Western Australia 2: Proceedings of the Petroleum Exploration Society of Australia Symposium, Perth, WA, p. 969-999.

Tentler, T., 2005, Propagation of brittle failure triggered by magma in Iceland: Tectonophysics, v. 406, no. 1, p. 17-38.

Trippanera, D., Acocella, V., Ruch, J., and Abebe, B., 2015a, Fault and graben growth along active magmatic divergent plate boundaries in Iceland and Ethiopia: Tectonics, v. 34, no. 11, p. 2318-2348.

Trippanera, D., Ruch, J., Acocella, V., and Rivalta, E., 2015b, Experiments of dike-induced deformation: Insights on the long-term evolution of divergent plate boundaries: Journal of Geophysical Research: Solid Earth, v. 120, no. 10, p. 6913-6942.

Tryggvason, E., 1984, Widening of the Krafla fissure swarm during the 1975–1981 volcano-tectonic episode: Bulletin of Volcanology, v. 47, no. 1, p. 47-69.

Vachon, R., and Hieronymus, C. F., 2017, Effect of host-rock rheology on dike shape, thickness and magma overpressure: Geophysical Journal International, v. 208, no. 3, p. 1414-1429.

Wilson, L., and Head, J. W., 2002, Tharsis-radial graben systems as the surface manifestation of plume-related dike intrusion complexes: Models and implications: Journal of Geophysical Research: Planets, v. 107, no. E8 5057.

Xu, W., Jónsson, S., Corbi, F., and Rivalta, E., 2016, Graben formation and dike arrest during the 2009 Harrat Lunayyir dike intrusion in Saudi Arabia: Insights from InSAR, stress calculations and analog experiments: Journal of Geophysical Research: Solid Earth, v. 121, no. 4, p. 2837-2851.

Supplementary Text

Sources of Error

There are several sources of error affecting confidence in quantitative measurements obtained from seismic reflection data. The primary error source in this study relates to seismic velocities used to convert the seismic data and measurements from depth in seconds two-way time (TWT) to depth in metres (see Magee and Jackson, 2020). This uncertainty arises because seismic velocities are obtained from borehole data, which effectively only provide a 1D snapshots of the subsurface geology and may thus not capture lateral variations in rock properties and seismic velocity. The numerous wells in our study area all display similar time-depth relationships, which indicates seismic velocities remain relatively constant laterally (Supplementary Figure 2). We thus take a conservative view that calculated seismic velocities vary by up to ±10%. Measurements of limits of separability and visibility, fault cut-offs, fault dips, dike upper tip, and dike lower tip depths rely on depth-converting time data and are therefore considered to have errors of ±10%. We also acknowledge that manual mapping and measurement can introduce human errors; we cannot quantify these errors but conservatively assume they could be up to ±5%. Fault dip data were extracted by creating dip angle maps from depth-converted fault surfaces constructed using all footwall cut-offs mapped along HA–HK (~1500 per fault). The convergent interpolation gridding algorithm in Schlumbergers's Petrel seismic interpretation software was used to grid these data into a surface; this algorithm applies a linear projection to extrapolate between points and a 'trend' method to preserve data trends. Overall, data for graben half-width (*HW*) and dike width are presented with ±5% errors as they do not rely on depth-converting any measurements, whilst the dikes lower and upper tip depths (including *D* and *D'*), fault dips, displacement, and heave assume errors are ±15%. Fault displacement and dip maps may also contain interpolation errors derived from our choice gridding algorithms, but we consider these negligible given the high density of measurement locations across both faults.

Supplementary data tables, figures, and videos are available on request.

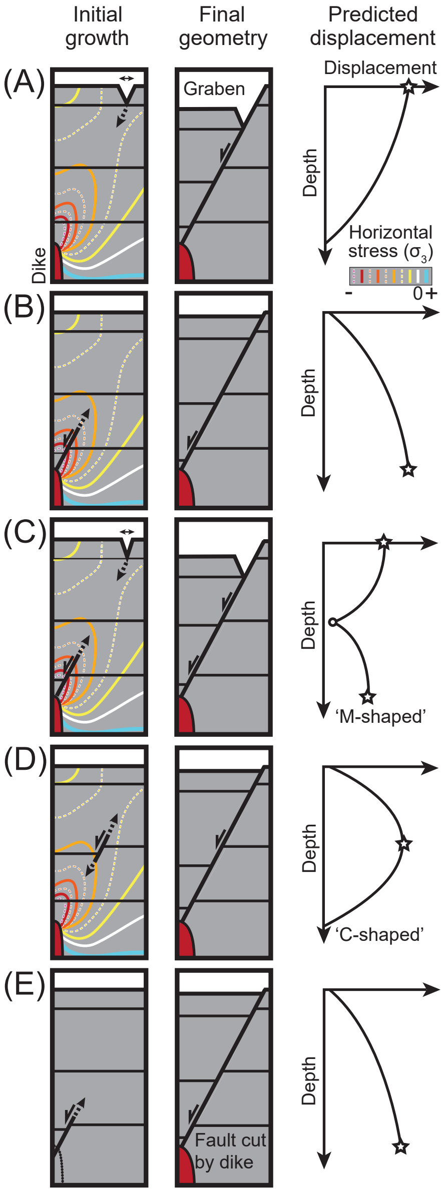
Initial growth
Final geometry
Predicted displacement
(A)
Graben
Displacement
Depth
Dike
Horizontal stress (σ_3)
-
0+
(B)
Depth
(C)
Depth
'M-shaped'
(D)
Depth
'C-shaped'
(E)
Depth
Fault cut by dike

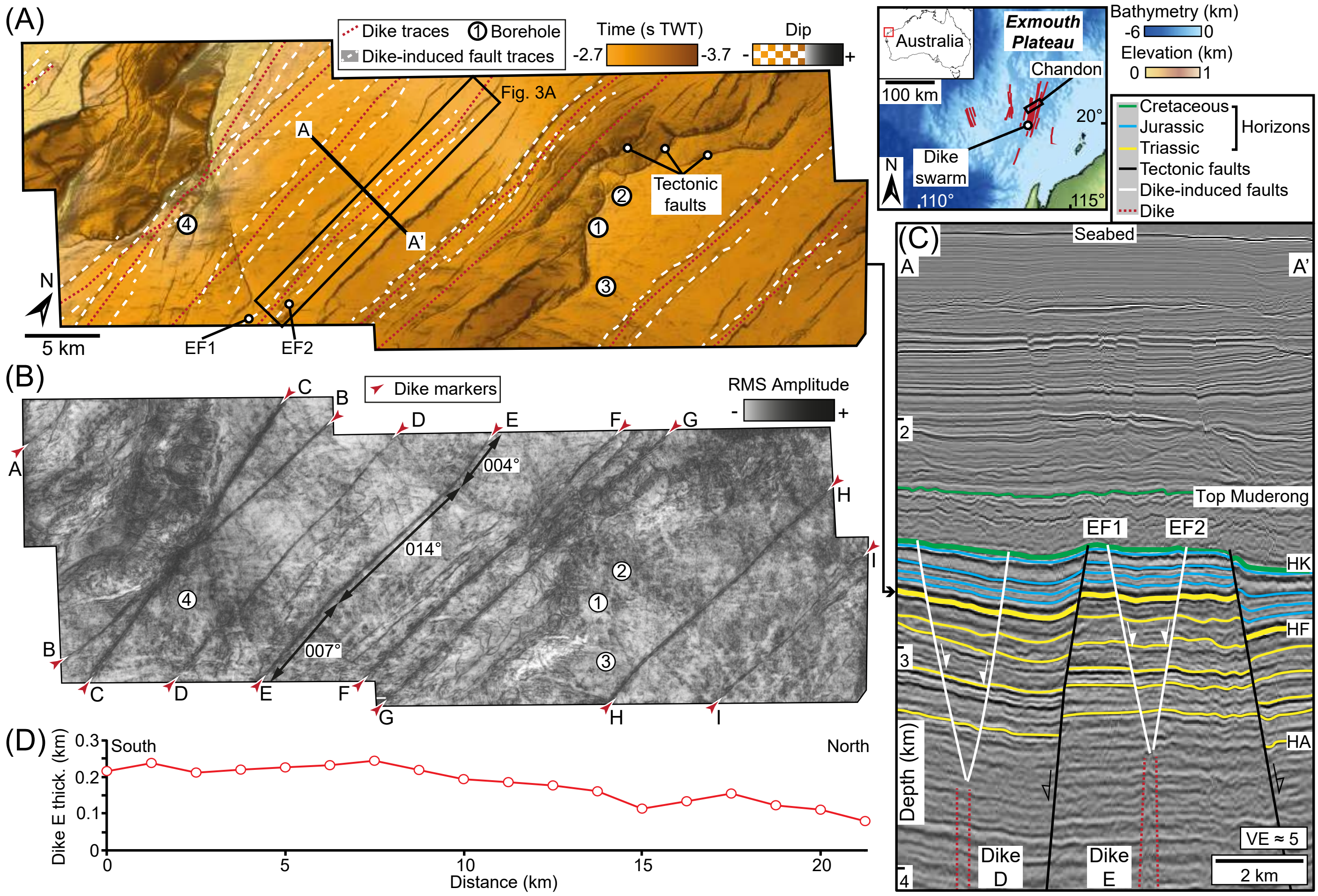
(A)
Dike traces
① Borehole
Dike-induced fault traces
Time (s TWT)
-2.7
-3.7
Dip
-
+
Fig. 3A
A
A'
Tectonic faults
②
①
③
④
N
5 km
EF1
EF2
Australia
Exmouth Plateau
Chandon
100 km
20°
Dike swarm
N
110°
115°
Bathymetry (km)
-6
0
Elevation (km)
0
1
Cretaceous
Jurassic
Triassic
Horizons
Tectonic faults
Dike-induced faults
Dike
(B)
Dike markers
RMS Amplitude
-
+
A
B
C
D
E
F
G
H
I
004°
014°
007°
(C)
Seabed
A
A'
2
Top Muderong
EF1
EF2
HK
HF
3
HA
Depth (km)
Dike D
Dike E
VE ≈ 5
2 km
4
(D)
Dike E thick. (km)
0.3
0.2
0.1
0
South
North
0
5
10
15
20
Distance (km)

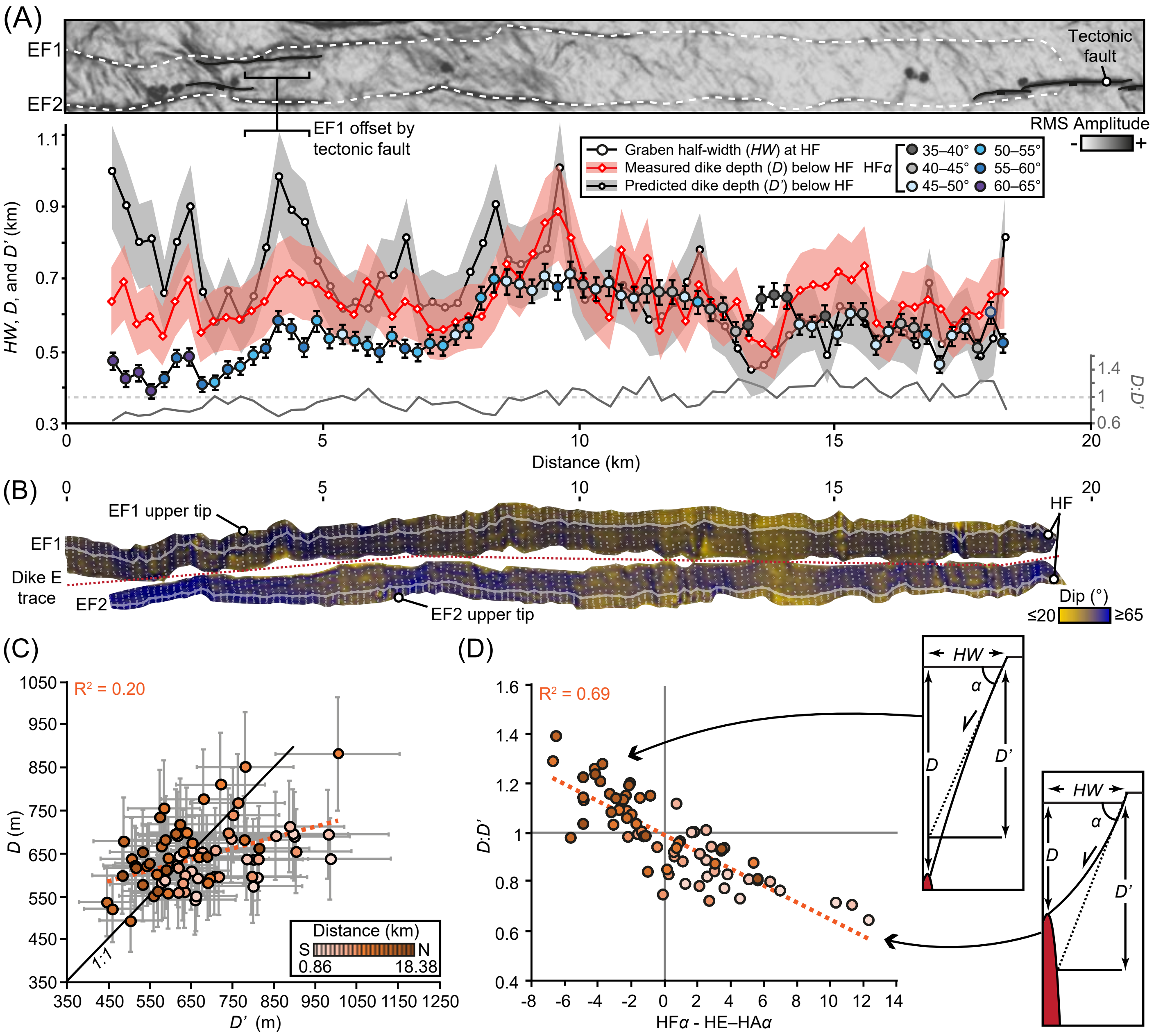
(A)
EF1
EF2
Tectonic fault
EF1 offset by tectonic fault
RMS Amplitude
- +
Graben half-width (HW) at HF
Measured dike depth (D) below HF
Predicted dike depth (D') below HF
HFα
35–40°
40–45°
45–50°
50–55°
55–60°
60–65°
HW, D, and D' (km)
D:D'
Distance (km)
0
5
10
15
20
0.3
0.5
0.7
0.9
1.1
0.6
1
1.4
(B)
EF1 upper tip
EF1
Dike E trace
EF2
EF2 upper tip
HF
Dip (°)
≤20
≥65
(C)
R² = 0.20
D (m)
D' (m)
1:1
Distance (km)
S
N
0.86
18.38
350
450
550
650
750
850
950
1050
1150
1250
(D)
R² = 0.69
D:D'
HFα - HE–HAα
-8
-6
-4
-2
0
2
4
6
8
10
12
14
0.4
0.6
0.8
1
1.2
1.4
1.6
HW
α
D
D'

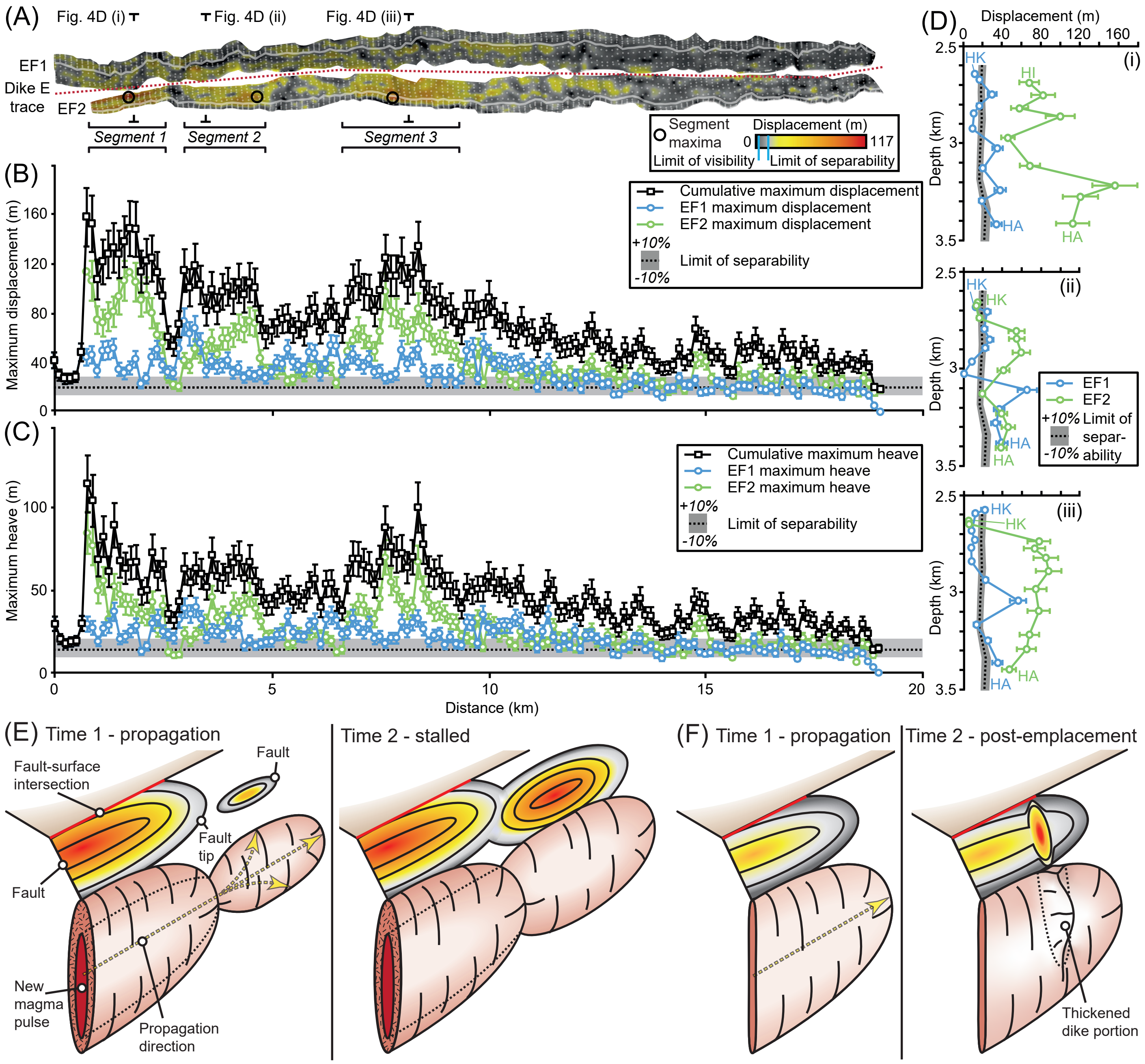
(A)
Fig. 4D (i)
Fig. 4D (ii)
Fig. 4D (iii)
EF1
Dike E trace
EF2
Segment 1
Segment 2
Segment 3
Segment maxima
Displacement (m)
0
117
Limit of visibility
Limit of separability
(B)
Maximum displacement (m)
160
120
80
40
0
Cumulative maximum displacement
EF1 maximum displacement
EF2 maximum displacement
+10%
-10%
Limit of separability
(C)
Maximum heave (m)
100
50
0
Cumulative maximum heave
EF1 maximum heave
EF2 maximum heave
+10%
-10%
Limit of separability
0
5
10
15
20
Distance (km)
(D)
Displacement (m)
0
40
80
120
160
(i)
Depth (km)
2.5
3
3.5
HK
HI
HA
HA
(ii)
HK
HK
HA
HA
EF1
EF2
+10% Limit of separ- ability
-10%
(iii)
HK
HK
HA
HA
(E) Time 1 - propagation
Fault-surface intersection
Fault
Fault tip
Fault
New magma pulse
Propagation direction
Time 2 - stalled
(F) Time 1 - propagation
Time 2 - post-emplacement
Thickened dike portion